Single-mask fabrication of sharp SiO_x nanocones (2023)

Eric Herrmann and Xi Wang

Abstract—The patterning of silicon and silicon oxide nanocones onto the surfaces of devices introduces interesting phenomena such as anti-reflection and super-transmissivity. While silicon nanocone formation is well-documented, current techniques to fabricate silicon oxide nanocones either involve complex fabrication procedures, non-deterministic placement, or poor uniformity. Here, we introduce a single-mask dry etching procedure for the fabrication of sharp silicon oxide nanocones with smooth sidewalls and deterministic distribution using electron beam lithography. Silicon oxide films deposited using plasma-enhanced chemical vapor deposition are etched using a thin alumina hard mask of selectivity > 88, enabling high aspect ratio nanocones with smooth sidewalls and arbitrary distribution across the target substrate. We further introduce a novel multistep dry etching technique to achieve ultra-sharp amorphous silicon oxide nanocones with tip diameters of ~10 nm. The processes presented in this work may have applications in the fabrication of amorphous nanocone arrays onto arbitrary substrates or as nanoscale probes.

Index Terms—angled sidewalls, dry etch, nanocones, silica, silicon oxide, single-mask

I. INTRODUCTION

THE advancement of nanofabrication has enabled complex technologies that utilize nanostructures (NSs) for subwavelength optics and nanoscale local probes. While optical devices such as waveguides and photonic crystals typically require smooth and vertical sidewalls for performance optimization and reduced sidewall scattering, many arising technologies have introduced variation of the NS morphology as an additional degree of freedom for tuning device functionality. Of significant importance are nanocones, which rely on the ability to fabricate NSs with tapered sidewalls. When patterned into arrays, subwavelength nanocones behave as a material with gradient refractive index, progressively bending incident light into the substrate onto which the nanocones are patterned [1], [2]. Recently, silicon (Si) and silica nanocones have attracted tremendous interest for applications in anti-reflection and anti-fogging coatings

This work was supported in part by the U.S. National Science Foundation under Grant 2128534. (Corresponding author: Xi Wang).

Eric Herrmann is with the Department of Materials Science & Engineering, University of Delaware, Newark, DE 19716 USA (e-mail: eherrm@udel.edu).

Xi Wang is with the Department of Materials Science & Engineering, University of Delaware, Newark, DE 19716 USA (e-mail: wangxi@udel.edu).

Color versions of one or more of the figures in this article are available online at http://ieeexplore.ieee.org

[3]–[8], drug-delivery systems [9], superhydrophobic surfaces [10], and surfaces for optical absorption enhancement [11], [12]. Si nanocones in particular have been thoroughly investigated due to the maturity of Si nanofabrication processing and the direct application of anti-reflecting nanocones to solar cells. Si NS morphology is strongly dependent on the method of fabrication. For example, while anisotropic wet chemical etching in potassium hydroxide produces Si pyramids with sidewall angles of 54.7°, metalassisted chemical etching has been widely adopted in the fabrication of black Si and a wide variety of other Si NSs [13]. [14]. In addition to wet etching techniques, inductivelycoupled plasma (ICP) reactive ion etching (RIE) incorporating fluorinated compounds enables both isotropic and anisotropic dry etching to achieve a variety of Si NS morphologies. While the well-known Bosch process utilizes alternating steps of fluorocarbon film passivation followed by isotropic dry etching for high-aspect-ratio vertical Si structures, isotropic dry etching in ICP followed by an oxidative sharpening process enables the formation of sharp silicon probes for atomic force microscopy [15]–[17]. The extension of ICP RIE to the cryogenic regime [18] has enabled the fabrication of Si NSs with smooth profiles and tunable sidewall angle while avoiding sidewall scalloping introduced by the Bosch process [19], [20]. More sophisticated combinations of dry etching oxidative sharpening followed by techniques successfully produced Si nanocones, nanopillars, and nanopencils with high aspect ratios and sharp tips, extending the control over the Si NS morphology even further [21]–[24].

1

While Si nanocone fabrication is well understood, silica nanocone formation is limited by current fabrication techniques. Silica nanocones exhibit remarkable physical and optical properties that enable broadband super-transmissivity [25], [26], super-hydrophobicity [10], [27], ultra-low diffuse reflectance and anti-fogging [28], and templates for hot electron photodetection [29]. With the exception of [25], these investigations utilize nanosphere lithography or techniques resulting in random distribution of silica nanocones. While these methods are superior for high-throughput manufacturing, they limit the tunability of the nanostructured surface. Although hybrid Si/SiO2 NSs can be fabricated by thermal oxidation of Si [30], [31], the oxide growth on sidewalls alters the morphology of NSs and high temperatures place limitations on process integration. Many RIE etching processes have been developed to achieve tapered silica sidewalls by varying temperature and etching gases [32]–[35], these studies employed photolithography-defined masks and applicability of these processes to the fabrication of NSs was

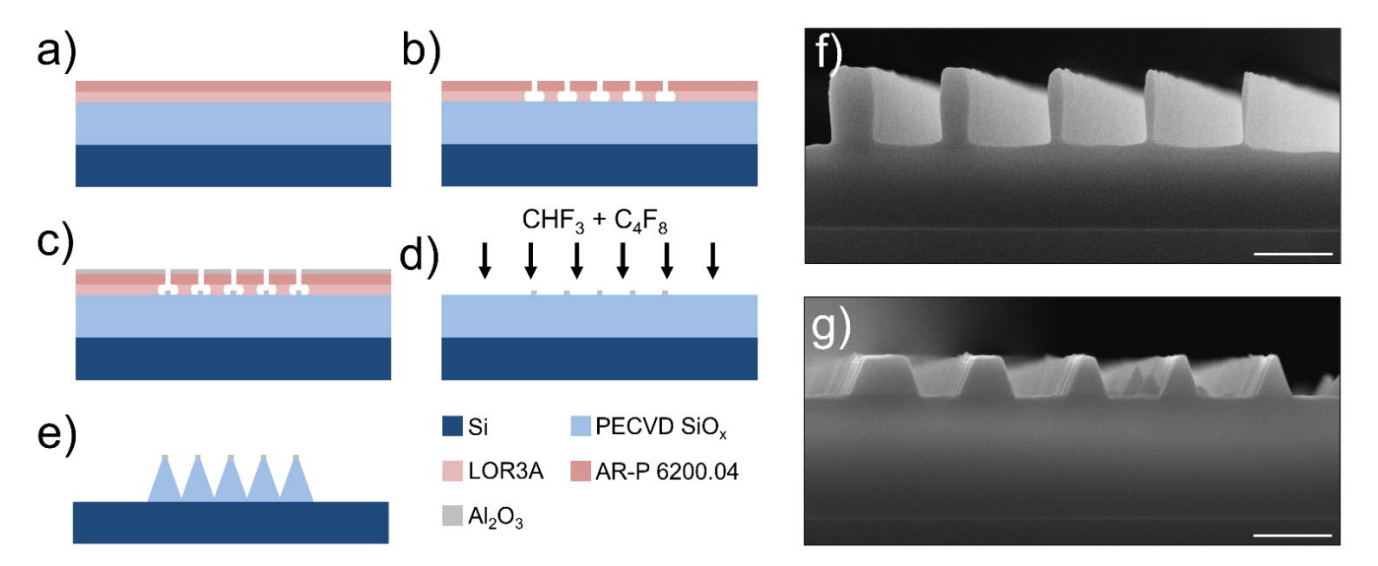


Fig. 1. Fabrication procedure of SiO_x nanocones. (a) The 1-μm-thick PECVD SiO_x film is deposited on a Si substrate and a bilayer resist is spun on top. (b) The resist is then exposed using electron beam lithography followed by development of the resist. (c) Deposition of alumina hard-mask using electron beam evaporation. (d) Following liftoff of the hard-mask material, samples are placed into an ICP chamber and etched in a dual-gas mixture of CHF₃ and C₄F₈. (e) The resulting SiO_x nanocones. Cross-sectional scanning electron microscope image of the SiO_x sidewall profiles for a (f) vertical and (g) nanocone etch. From left to right, the in-plane widths of the alumina hard masks used to form the structures are 300, 200, 100, 80, and 60 nm. Both scale bars are 500 nm.

not explored. Furthermore, to the best of our knowledge, all previous investigations of silica nanostructures have been fabricated using thermally-grown SiO₂ or fused silica wafers, limiting process integration to specific substrate materials.

In this paper, we report a single-mask dry etching process for sharp plasma-enhanced chemical vapor deposited silicon oxide nanocones (pSONs). Plasma-enhanced chemical vapor deposition (PECVD) enables the fabrication of silicon oxide (SiO_x) nanocones onto unconventional substrates beyond fused silica and thermally-oxidized silicon. The dual-gas CHF₃ + C₄F₈ procedure yields smooth and repeatable pSONs with tip diameters approaching the resolution limits of conventional electron beam lithography (EBL) systems. We further extend our investigation to an all-dry multi-step ICP etching process for ultra-sharp pSONs with tip diameters of ~10 nm. The pSONs presented in this work may have applications as subwavelength optical elements or nanoscale probes across a variety of disciplines.

II. RESULTS

The pSON fabrication sequence is summarized in Figs. 1(a)-(e). 1 µm thick silicon oxide films were deposited at 300°C onto pre-cleaned Si substrates using PECVD (Plasma-Therm Versaline). We utilize a bilayer resist procedure for improved liftoff performance of the hard-mask. Liftoff resist (LOR3A, Kayaku Advanced Materials, Inc.) and positive-tone electron beam resist (AR-P 6200.04, Allresist) were spun onto the sample and subsequently exposed using electron beam lithography (EBL, Raith EBPG5200ES) to write structures between 50-300 nm in width. Patterns consisting of 3mm-long lines of various widths were written for formation of pSON

wedges and cross-sectional scanning electron microscopy (SEM). Circular patterns were defined for pSON formation. Following development of the resists, samples were placed into an oxygen plasma asher (Branson/IPC 3000) to remove resist residuals. A 40-nm-thick alumina hard-mask was then deposited using electron-beam evaporation (PVD Products), followed by liftoff of excess alumina.

Anisotropic dry-etching of the SiO_x films was performed in a fluorine-based ICP (F-ICP) system (F-ICP, Plasma-Therm Apex SLR) with the carrier wafer held at 20°C. Prior to placing samples in the chamber, the F-ICP chamber was cleaned in oxygen plasma for 10 minutes. Samples were then placed in the chamber and etching gases were allowed to flow through the chamber for 5 minutes prior to sparking the plasma to ensure flushing of contaminant gases. We first present cross-sectional SEM images comparing the profiles of vertical and tapered etches in Figs. 1(f) and (g), respectively. In both cases, the total etch time was 4 minutes. From left to right, the in-plane widths of the deposited alumina hard-masks are 300, 200, 100, 80, and 60 nm. The vertical sidewall profiles in Fig. 1(f) were achieved by flowing CHF₃ and O₂ at rates of 45 and 5 sccm, respectively, while holding a chamber pressure of 8 mTorr. The RF power was set to 30W while the ICP power was set to 600W. The vertical etching process has an etch rate of ~1.98 nm/s and results in nanostructures with relatively vertical sidewalls but slight undercutting near the base of the etch. To achieve a tapered etch as in Fig. 1(g), we

replace O₂ with C₄F₈ and set the flow rates of CHF₃ and C₄F₈

to 30 and 40 sccm, respectively. The RF power was set to

30W, the ICP power to 300W, and the chamber pressure to 8

mTorr. The power density within the ICP chamber during the

1

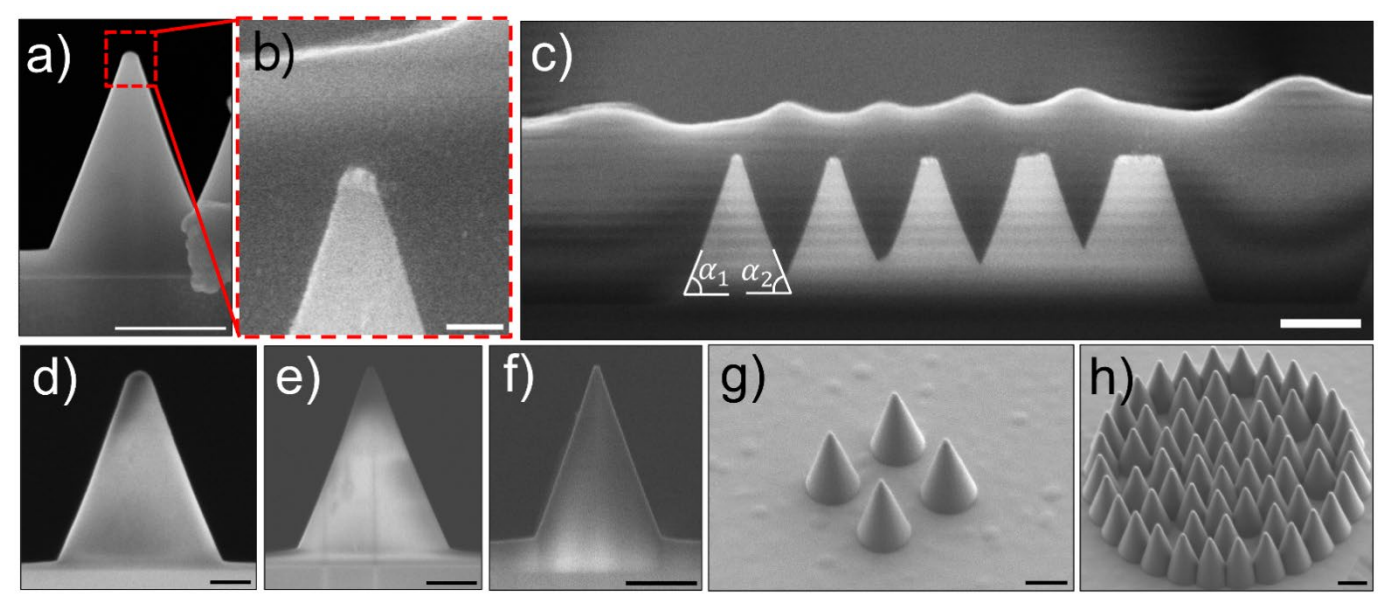


Fig. 2. PECVD SiO_x nanocones fabricated using fluorine-based inductively coupled plasma etching. (a) Cross-sectional scanning electron microscope (SEM) image of the nanocone profile. The piece of debris in the lower right corner of the image is a result of cleaving the sample. Scale bar, 500 nm. (b) A photoresist-covered nanocone tip showcasing the remaining alumina hard-mask after 16 minutes of etching. The slanted white line near the top of the figure is the photoresist/air boundary. Scale bar, 100 nm. (c) Zoomed-out SEM image of structure in (b) demonstrating the etch-stop behavior at intersections between neighboring sidewalls. The width of alumina mask from left to right is 60, 80, 100, 200, and 300 nm. Scale bar, 500 nm. Cross-sectional SEM images of pSONs etched from (d) 1 μm (e) 2 μm and (f) 3 μm thick SiO_x films. The scale bars of (d), (e), (f) are 200, 500, and 1000 nm, respectively. (g) Nanocones located at the four corners of square of width 1 μm. The sidewall and baseline of the etch are smooth. Scale bar, 500 nm. (h) Complex design of patterned nanocones showcasing repeatability of nanocone morphology. Scale bar, 500 nm.

tapered etch is $\sim 1.6 \text{W/cm}^2$ and the substrate-induced bias voltage is $\sim 97 \text{V}$. Compared to the vertical etch, the tapered etch is significantly slower at a rate of ~ 0.95 nm/s and results in pSON wedges with linear sidewalls of angle ~ 70 degrees.

III. DISCUSSION

All fabricated samples underwent SEM imaging to confirm the uniformity of patterned pSON distributions, which was determined to be excellent, limited mainly by the capabilities of the EBL system and the optimization of exposure recipes. Fig. 2(a) shows an up-close cross-sectional SEM image of a pSON wedge formed after increasing the tapered etch time to 16 minutes. Using SEM, we measure an SiO_x etch depth of roughly 880 nm giving an etch rate of 0.92 nm/s, in excellent agreement with the etch rate measured after a 4 minute etch. This indicates that the etch depth scales linearly with time and pSONs of arbitrary height can be fabricated provided the etch selectivity is sufficient. A second sample was fabricated using identical etching conditions, covered with photoresist, and imaged at a lower accelerating voltage to improve contrast between the alumina hard mask and pSON wedge. Fig. 2(b) shows the sharp rounded tip prior to removal of the hard mask. As can be seen in Figs. 2(b) and (c), there does not appear to be any undercutting of the alumina hard-mask, indicating that much sharper pSONs may be achievable by decreasing the in-plane width of the hard-mask even further. We use SEM to roughly measure the remaining thickness of the alumina hard-mask following the etch and find

that greater than 30 nm remains, which gives a selectivity of >88. The low etch rate of alumina in ICP RIE involving passivating fluorocarbons is well known [36], [37] and, together with the absence of undercut observed, may enable extremely sharp pSONs with very high aspect ratio, limited only by resolution limits of EBL. However, the slow etch rate of the presented pSON etch process, along with stability of high aspect ratio masks, may affect the limitations of such structures.

An expanded view of Fig. 2(b) is shown in Fig. 2(c) and shows the result of etching closely-spaced patterns of varying widths. The widths of the defined hard-masks from left to right are 60, 80, 100, 200, and 300 nm. We measure all sidewall angles α throughout the structure (e.g. α_1 and α_2 in Fig. 2(c) are the two sidewall angles measured for the left-most wedge structure) and find that variation in sidewall angle across the pattern is less than 3 degrees. The spacing-dependent etch depth between neighboring structures, also known as RIE lag, may be due to insufficient recycling of reactive species or trapping of passivating fluorocarbon film within the trenches. We note that, because the plane where two neighboring sidewalls intersect behaves as an etch-stop, the bottoms of the trenches are extremely sharp. Closely-spaced pSONs may therefore be employed as nano-imprint lithography stamps resulting in very sharp structures of varying height dependent on the spatial variation of structures within the stamp.

Multiple SiO_x films were prepared to investigate the depth-

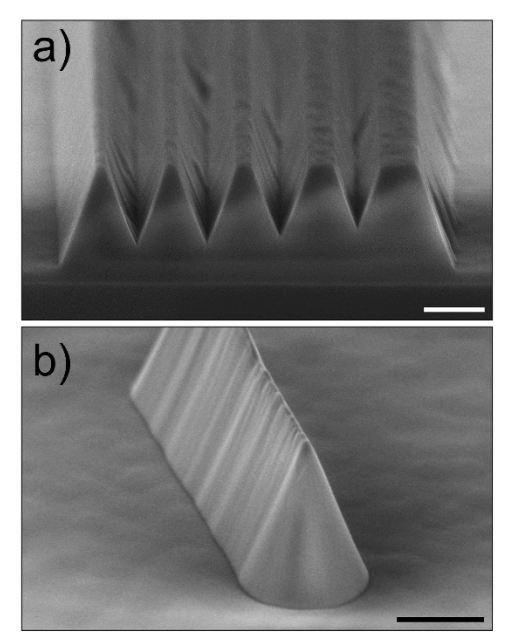


Fig. 3. (a) Tilted cross-sectional SEM image of closely spaced nanostructures emphasizing sidewall rippling. Scale bar, 500 nm. (b) Tilted SEM image of a truncated pSON wedge. Sidewall rippling correlates with local fluctuations in the SiO_x thickness. The ends of the pSON wedge are terminated with one-half of a pSON with smooth sidewalls. Scale bar, 1 μ m.

dependent etching rates and sidewall angle dependence on the aspect ratio of fabricated pSON wedges. SiO_x films of thickness 1, 2, and 3 µm were considered and the resulting pSON wedges are shown in the cross-sectional SEM images in Figs. 2(d)-(f), respectively. The sidewall angles of the resulting nanostructures were measured to be ~70 degrees, indicating that the sidewall angle is independent of etching depth. The pSONs in Fig. 2(g) are the result of etching SiO_x with circular alumina masks placed at the four corners of a square and demonstrate both smooth sidewalls and etch baseline relative to the closely-spaced pSON wedges. pSONs patterned with variation in the pSON density and sidewall overlap are shown in Fig. 2(h), revealing that our fabrication process provides a method for fabricating repeatable high-quality pSONs with highly deterministic placement.

While fabricated pSONs exhibit smooth sidewalls, we observe undesirable rippling along the sidewalls of etched pSON wedges. Fig. 3(a) is a tilted cross-sectional SEM image showcasing this rippling behavior both within the trenches and along the outermost sidewalls of the pattern. To elucidate the origin of sidewall rippling, we fabricated truncated pSON wedges using the tapered etch procedure and display the result in the tilted SEM image of Figure 3(b). The truncated pSON wedge exhibits rippling along the sidewalls while the truncated end of the forms one-half of a nanocone with smooth sidewalls. The rippling along the sidewalls originates from local fluctuations in the SiO_x film thickness, leading to local protrusions and depressions for regions that are slightly thicker and thinner, respectively. Optimization of the PECVD deposition conditions to decrease surface roughness may mitigate the sidewall rippling effect.

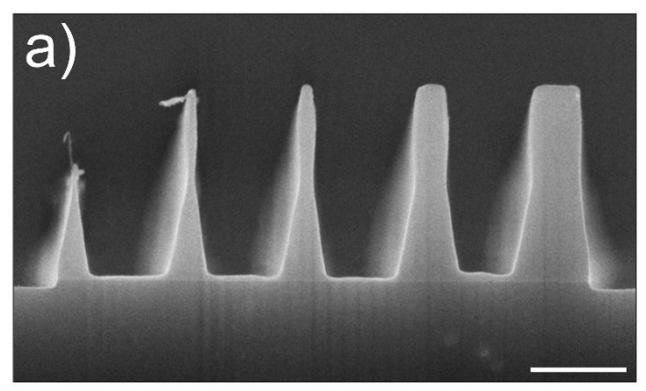
Lastly, we present a novel all-dry etch process to fabricate

ultra-sharp pSONs with tip diameters of ~10nm. This proof-ofconcept process is achieved by utilizing four F-ICP etching steps without removing the sample from the chamber. After repeating the deposition and lithography process as described in Figs. 1(a)-(c), we first run the tapered etch process for 4 minutes. Without cleaning the chamber with O₂ plasma and after purging all gases, we then run the vertical etch process as described for Fig. 1(f) for 2 minutes. We then repeat this two-step etch a second time and present a cross-sectional SEM image of the final structure in Fig. 4(a). The in-plane widths of the defined hard-masks are the same as described for Fig. 2(c) and the resulting sidewall profile can be described by two separate regions. The top-half of the etched pSON wedges are nearly vertical with a slight undercut toward the middle of the wedge, while the bottom half has a tapered edge. As the width of the hard-mask decreases, the middle of the pSON wedges experience more significant "necking" until a full undercut occurs at the center of the structures defined by a 60nm-wide alumina hard mask. The remaining bottom half of the structure is an ultra-sharp pSON wedge of height ~500 nm, half the height of the original SiO_x film. While only the 60 nm hardmask experiences a full undercut, the same etch process produces ultra-sharp pSONs from both the 80- and 100-nm-wide hardmasks, as shown by the arrays on the left- and right-side of Fig. 4(b), respectively. Although not shown, pSONs from the 60-nmwide hard-masks are destroyed because they are formed at some point during the ongoing etching process and are "blunted" by the continuation of etching. Fig. 4(c) is a zoomed-in image of the pSON apex and depicts a smooth sidewall terminated by an ultrasharp tip of ~10 nm. This necking and fracture process is similar to that described in the fabrication of silicon AFM probes [7], [8] without the requirement of a wet etching process for final formation. To the best of our knowledge, this is the first demonstration of ultra-sharp nanostructures fabricated using amorphous materials. We anticipate that further experimentation of combining etching steps will enable precise control over the morphology of pSON sidewalls.

V. CONCLUSION

In summary, we describe a novel single-mask all-dry etching procedure to fabricate sharp SiO_x nanocones that may have applications in optical systems or as nanoscale probes. Our process involves a dual CHF3 and C4F8 gas mixture and utilizes an electron-beam evaporated alumina hard mask with selectivity >88, enabling sharp and high-aspect-ratio nanocones with smooth sidewalls and arbitrary distribution defined by electron beam lithography. Our PECVD-SiO_x nanocones facilitate the fabrication of transparent dielectric nanocone distributions onto unconventional films and substrates when fused silica and thermally-oxidized silicon are unavailable. We further describe a novel process to achieve ultra-sharp amorphous nanocones by alternating dry-etching recipes without removing the sample from the ICP chamber and achieve nanocone apex diameters of ~10 nm or less. The formation of ultra-sharp nanocones involves a full undercut of nanopillars at mid-height, resulting in nanocones of height equal to roughly half of the initially-deposited film.

While the PECVD deposition temperature of SiO_x films



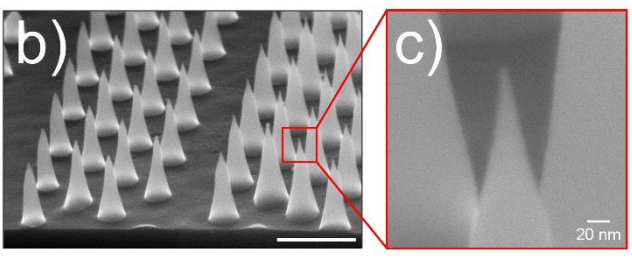


Fig. 4. (a) Cross-sectional SEM image following multi-step ICP etching for 60, 80, 100, 200, and 300 nm wide alumina hard-masks. Scale bar, 500 nm. (b) Tilted SEM image of ultra-sharp nanocone arrays (Scale bar, 500nm) and (c) a zoomed-in image of the nanocone tip of radius ~10 nm. Scale bar, 20 nm.

reported in this work is 300° C, we anticipate that our process may be extended to low-temperature PECVD grown SiO_x films for nanocone formation on polymer-based and flexible substrates, which may have applications in functionalized needle arrays for drug delivery or flexible optical devices.

Furthermore, because our process only involves a single mask, the described nanocone fabrication procedure may be extended to nanosphere lithography to enable high throughput manufacturing. Finally, it would be interesting to investigate the extension of our ultra-sharp nanocone fabrication process to photolithography techniques. Because the undercutting process results in nanocone tips of diameter much smaller than the initial mask size, optimization of the undercutting process may enable sharp nanostructure fabrication by undercutting of masks defined using photolithography.

ACKNOWLEDGMENT

The authors give special thanks to Shyan-Tzong "Paul" Horng, Ph.D., of the University of Delaware Nanofabrication Facility (UDNF) for maintaining the inductively-coupled plasma dry etching systems and engaging in valuable discussions pertaining to processing a variety of materials. The authors also thank other UDNF staff including Iulian Codreanu, Ph.D., Scott McCracken, Zhichao Wang, Ph.D., and Angeline Briscoe for enabling an atmosphere that stimulates efficient research and fruitful discussion.

REFERENCES

 J. Cai and L. Qi, "Recent advances in antireflective surfaces based on nanostructure arrays," Mater. Horizons, vol. 2, no. 1, pp. 37–53, 2015, doi: 10.1039/C4MH00140K.

- [2] Z. Han, Z. Jiao, S. Niu, and L. Ren, "Ascendant bioinspired antireflective materials: Opportunities and challenges coexist," Prog. Mater. Sci., vol. 103, no. May 2018, pp. 1–68, 2019, doi: https://doi.org/10.1016/j.pmatsci.2019.01.004.
- [3] Y. Zhao et al., "Broadband omnidirectional anti-reflection property of V-groove textured silicon", Solar Energy, vol. 193, pp. 132–138, Nov. 2019, doi: 10.1016/j.solener.2019.09.048.
- [4] Y. Yamada, H. Iizuka, and N. Mizoshita, "Silicon Nanocone Arrays via Pattern Transfer of Mushroomlike SiO2 Nanopillars for Broadband Antireflective Surfaces", ACS Appl Nano Mater, vol. 3, no. 5, pp. 4231– 4240, May 2020, doi: 10.1021/acsanm.0c00417.
- [5] K. Xu, J. Hu, M. Wang, G. J. Cheng, and S. Xu, "Armored Nanocones Engraved by Selective Laser Doping Enhanced Plasma Etching for Robust Supertransmissivity", ACS Appl Mater Interfaces, vol. 14, no. 41, pp. 47237–47245, Oct. 2022, doi: 10.1021/acsami.2c13033.
- [6] J. Rombaut, S. Martínez, U. M. Matera, P. Mazumder, and V. Pruneri, "Antireflective Multilayer Surface with Self-Cleaning Subwavelength Structures", ACS Photonics, vol. 8, no. 3, pp. 894–900, Mar. 2021, doi: 10.1021/acsphotonics.0c01909.
- [7] S. M. Yoon, Y. A. Lee, K. C. Park, S. Nahm, and M. W. Moon, "Subwavelength Hollow-Nanopillared Glass with Gradient Refractive Index for Ultralow Diffuse Reflectance and Antifogging", ACS Appl Mater Interfaces, vol. 12, no. 5, pp. 6234–6242, Feb. 2020, doi: 10.1021/acsami.9b19228.
- [8] K. X. Wang, Z. Yu, V. Liu, Y. Cui, and S. Fan, "Absorption enhancement in ultrathin crystalline silicon solar cells with antireflection and light-trapping nanocone gratings", *Nano Lett*, vol. 12, no. 3, pp. 1616–1619, Mar. 2012, doi: 10.1021/nl204550q.
- [9] B. Liu et al., "A Review of Nano/Micro/Milli Needles Fabrications for Biomedical Engineering", Chin. J. Mech. Eng., vol. 35, no. 1. Springer, Dec. 2022. doi: 10.1186/s10033-022-00773-6.
- [10] K. C. Park, H. J. Choi, C. H. Chang, R. E. Cohen, G. H. McKinley, and G. Barbastathis, "Nanotextured silica surfaces with robust superhydrophobicity and omnidirectional broadband supertransmissivity", ACS Nano, vol. 6, no. 5, pp. 3789–3799, May 2012, doi: 10.1021/nn301112t.
- [11] J. Sullivan, Z. Yu, and J. Lee, "Nanometer-Thick Nickel Coatings on Silicon Micropyramids for Infrared Absorption", ACS Appl Nano Mater, vol. 5, no. 4, pp. 4615–4622, Apr. 2022, doi: 10.1021/acsanm.2c00541.
- [12] J. Zhu et al., "Optical absorption enhancement in amorphous silicon nanowire and nanocone arrays", Nano Lett, vol. 9, no. 1, pp. 279–282, Jan. 2009, doi: 10.1021/nl802886y.
- [13] H. Han, Z. Huang, and W. Lee, "Metal-assisted chemical etching of silicon and nanotechnology applications", *Nano Today*, vol. 9, no. 3, pp. 271–304, Apr. 2014, doi: 10.1016/j.nantod.2014.04.013.
- [14] J. Soueiti, R. Sarieddine, H. Kadiri, A. Alhussein, G. Lerondel, and R. Habchi, "A review of cost-effective black silicon fabrication techniques and applications", *Nanoscale*, vol. 15, no. 10, pp. 4738–4761, Feb. 2023, doi: 10.1039/d2nr06087f.
- [15] H. He, J. Zhang, J. Yang, and F. Yang, "Silicon tip sharpening based on thermal oxidation technology", *Microsyst Technol*, vol. 23, no. 6, pp. 1799–1803, Jun. 2017, doi: 10.1007/s00542-016-2941-0.
- [16] R. K. Dey, J. Shen, and B. Cui, "Oxidation sharpening of silicon tips in the atmospheric environment", *J. Vac. Sci. Technol. B*, vol. 35, no. 6, p. 06GC01, Nov. 2017, doi: 10.1116/1.4998561.
- [17] C. Y. Hong and A. I. Akinwande, "Oxidation sharpening mechanism for silicon tip formation", *Electrochem. Solid-State Lett*, vol. 8, no. 5, Apr. 2005, doi: 10.1149/1.1887190.
- [18] S. Tachi, K. Tsujimoto, and S. Okudaira, "Low-temperature reactive ion etching and microwave plasma etching of silicon", *Appl Phys Lett*, vol. 52, no. 8, pp. 616–618, Feb. 1988, doi: 10.1063/1.99382.
- [19] Z. Liu, Y. Wu, B. Harteneck, and D. Olynick, "Super-selective cryogenic etching for sub-10 nm features", *Nanotechnology*, vol. 24, no. 1, Jan. 2013, doi: 10.1088/0957-4484/24/1/015305.
- [20] V. Ishchuk, D. L. Olynick, Z. Liu, and I. W. Rangelow, "Profile simulation model for sub-50 nm cryogenic etching of silicon using SF6/O2 inductively coupled plasma", *J Appl Phys*, vol. 118, no. 5, Aug. 2015, doi: 10.1063/1.4927731.
- [21] H. Lin et al., "Rational design of inverted nanopencil arrays for cost-effective, broadband, and omnidirectional light harvesting," ACS Nano, vol. 8, no. 4, pp. 3752–3760, Apr. 2014, doi: 10.1021/nn500418x.
- [22] C. M. Hsu, S. T. Connor, M. X. Tang, and Y. Cui, "Wafer-scale silicon nanopillars and nanocones by Langmuir-Blodgett assembly and etching", *Appl Phys Lett*, vol. 93, no. 13, pp. 26–28, Oct. 2008, doi: 10.1063/1.2988893.

- [23] D. Jonker, E. J. W. Berenschot, N. R. Tas, R. M. Tiggelaar, A. van Houselt, and H. J. G. E. Gardeniers, "Large Dense Periodic Arrays of Vertically Aligned Sharp Silicon Nanocones", *Nanoscale Res Lett*, vol. 17, no. 1, Oct. 2022, doi: 10.1186/s11671-022-03735-y.
- [24] N. Kim, D. Choi, H. Kim, H. D. Um, and K. Seo, "Silicon Microwire Arrays with Nanoscale Spacing for Radial Junction c-Si Solar Cells with an Efficiency of 20.5%", vol. 15, no. 9. ACS Nano, 2021, pp. 14756– 14765. doi: 10.1021/acsnano.1c04585.
- [25] K. C. Park, H. J. Choi, C. H. Chang, R. E. Cohen, G. H. McKinley, and G. Barbastathis, "Nanotextured silica surfaces with robust superhydrophobicity and omnidirectional broadband supertransmissivity", ACS Nano, vol. 6, no. 5, pp. 3789–3799, May 2012, doi: 10.1021/nn301112t.
- [26] K. Xu, J. Hu, M. Wang, G. J. Cheng, and S. Xu, "Armored Nanocones Engraved by Selective Laser Doping Enhanced Plasma Etching for Robust Supertransmissivity", ACS Appl Mater Interfaces, vol. 14, no. 41, pp. 47237–47245, Oct. 2022, doi: 10.1021/acsami.2c13033.
- [27] Y. Li et al., "Bioinspired silica surfaces with near-infrared improved transmittance and superhydrophobicity by colloidal lithography", *Langmuir*, vol. 26, no. 12, pp. 9842–9847, Jun. 2010, doi: 10.1021/la100183y.
- [28] S. M. Yoon, Y. A. Lee, K. C. Park, S. Nahm, and M. W. Moon, "Subwavelength Hollow-Nanopillared Glass with Gradient Refractive Index for Ultralow Diffuse Reflectance and Antifogging", ACS Appl Mater Interfaces, vol. 12, no. 5, pp. 6234–6242, Feb. 2020, doi: 10.1021/acsami.9b19228.
- [29] Z. Yang *et al.*, "Silica nanocone array as a template for fabricating a plasmon induced hot electron photodetector", *Photonics Res*, vol. 7, no. 3, p. 294, Feb. 2019, doi: 10.1364/prj.7.000294.
- [30] E. Kim et al., "MoS2 monolayers on Si and SiO2 nanocone arrays: Influences of 3D dielectric material refractive index on 2D MoS2 optical absorption", Nanoscale, vol. 10, no. 40, pp. 18920–18925, Sep. 2018, doi: 10.1039/c8nr06597g.
- [31] T. Okatani, Y. Naito, and Y. Kanamori, "Fabrication of high-aspect-ratio SiO2 nanopillars by Si thermal oxidation for metalenses in the visible region", *Jpn J Appl Phys*, vol. 62, no. SG, Mar. 2023, doi: 10.35848/1347-4065/acbfbe.
- [32] A. G. Nagy, "Sidewall Tapering in Reactive Ion Etching," J Electrochem Soc, vol. 132, no. 3, pp. 689–693, Mar. 1985, doi: 10.1149/1.2113932.
- [33] V. Bliznetsov, B. Li, J. Wung Lee, and H. Lin, "MEMS industry-worth etching to fabricate tapered structures in SiO2", *J. Microelectromech. Syst.*, vol. 26, no. 6, pp. 1400–1407, Oct. 2017, doi: 10.1109/JMEMS.2017.2755046.
- [34] T. Ohiwa, K. Horioka, T. Arikado, I. Hasegawa, and H. O. Haruo Okano, "SiO 2 Tapered Etching Employing Magnetron Discharge of Fluorocarbon Gas," *Jpn J Appl Phys*, vol. 31, no. 2R, p. 405, Feb. 1992, doi: 10.1143/JJAP.31.405.
- [35] A. Behrens and S. Sinzinger, "2.5D+ plasma etching for a continuously adjustable sidewall angle in SiO2," Opt Mater Express, vol. 13, no. 6, p. 1780, Jun. 2023, doi: 10.1364/ome.484157.
- [36] M. Drost et al., "Etch mechanism of an Al2O3 hard mask in the Bosch process," Micro and Nano Engineering, vol. 14, pp. 100102, Apr. 2022, doi: 10.1016/J.MNE.2021.100102.
- [37] K. Kolari, "High etch selectivity for plasma etching SiO2 with AlN and Al2O3 masks," *Microelectron Eng*, vol. 85, no. 5–6, pp. 985–987, May 2008, doi: 10.1016/J.MEE.2007.12.037.